J. Fluid Mech. (1984), *vol.* 145, *pp.* 127–149
Printed in Great Britain

On the generation and evolution of internal gravity waves

By FAIZA S. LANSING† AND TONY MAXWORTHY‡
Departments of Mechanical and Aerospace Engineering, University of Southern California, Los Angeles, California 90089-1453

(Received 18 January 1983 and in revised form 5 March 1984)

In order to study the tidal generation and evolution of internal waves, both experimentally and theoretically, a two-dimensional two-layer model has been developed. The laboratory model consists of two immiscible fluid layers in a long wave tank, where time-dependent flow can be created by towing a suitably shaped obstacle with a sinusoidal motion. The effects of changing the Froude number and the ratio of the depths of the two fluid layers on the shape of the interface are studied. The first theoretical model considers the motion to be quasi-steady, allowing only a balance between buoyancy and inertial forces, and is in reasonable agreement with the experimental results for very slow motions and the initial phase of the tidal cycle only. A more complete numerical solution is based on the vortex-point method in which the interface is modelled by a set of discrete vortices, while the rigid boundaries, which include the obstacle, are modelled by a source distribution. The resulting governing equations are expressed in Lagrangian form, and the baroclinic generation of vorticity is related to the generation of source density, through two simultaneous integrodifferential equations. For small Froude numbers, the experimental and numerical results are in good quantitative agreement. At large Froude numbers, the numerical solution, which does not consider mixing between the two layers nor boundary-layer separation from the obstacle, gives a slight difference in the position of the maximum interface displacement from that found in the experiment.

1. Introduction

The existence of large-amplitude internal waves in the ocean has been noted by several authors (Halpern 1971; Gargett 1976; Smith & Farmer 1977; among many). In all cases it was clear that tidal interaction with bottom topography was the major source, although the exact sequence of events that created the waves was not clear. In an initial attempt to study this problem, Lee & Beardsley (1974) constructed an experimental model in which they postulated the generation of such waves during that part of the tidal cycle when the flow was in the direction of wave propagation. This possibility was criticized by Maxworthy (1979), who studied, experimentally, tidally generated solitary waves over a three-dimensional ridge, simulating the internal waves produced by flow over Stellwagen Bank in Massachusetts Bay. Maxworthy proposed a somewhat different sequence of events that leads to the production of an internal wave train. As the ebb tide proceeds, a depression, i.e. a lee wave, is formed behind the obstacle. The characteristics of this depression depend

† Present address: Tracking Systems and Applications Section, Jet Propulsion Laboratory, Pasadena, California 91109.
‡ Also Earth and Space Sciences Division, J.P.L., Pasadena, California 91109.

on the basic density stratification, the shape of the obstacle and the magnitude and direction of the tidal current. As the ebb tide slackens, the depression, which has gained a large potential energy, moves upstream against the flow. As the depression propagates away from the obstacle it evolves into a number of solitary waves. The number and amplitude of these waves depend on the characteristics of the depression and basic density stratification.

This generation mechanism has succeeded in explaining the production of solitary waves observed by Halpern (1971) and Chereskin (1983) in Massachusetts Bay and Gargett (1976) in the strait of Georgia. Also, the field observation of Apel and Holbrook (Apel & Holbrook 1980; Holbrook & Apel 1980) in the Sulu Sea and Osborne & Burch (1980) in the Andaman Sea support this mechanism as an explanation for the production of the internal-wave packets as shown for the former measurements by Liu (1982).

It was suggested that this description was also applicable to some of the field observations by Smith & Farmer (1977) in Knight Inlet, as shown in the acoustic radar images of the flow over a sill in the fjord and the observation of solitary waves propagating away from this location. However, Farmer & Smith (1980) argued that there are probably at least two different generation mechanisms. The exact response of the flow over the sill mainly depended upon the stratification and the strength of the tidal currents. The first-generation mechanism involved the formation of an internal lee-wave train and the second involved the formation of a single lee wave behind the sill. The latter response is similar to the internal hydraulic jump discussed by Long (1954). In the former case lee-wave train formation was described as follows: the time-dependent interaction with boundary-layer separation occurred in the early stages of the tide, followed by the formation of lee waves that had a suitable form to suppress separation. Successive lee waves formed behind the first one. Their characteristics depend on the tidal current and stratification. As the tide slackened, the first wave propagated upstream, passing over the obstacle, and was replaced by new waves forming in the lee of the obstacle. These waves controlled the location of separation of the boundary layer by modifying the flow over the leeside of the sill. The waves travelled upstream as a packet and evolved either into turbulent breaking waves or solitary waves that obeyed the nonlinear dispersive theory. The main disagreement with Maxworthy's generation mechanism is whether the waves are generated by the disintegration of a single large depression or if during generation a train of lee waves is formed behind the obstacle as the flow velocity drops, which then propagate away from the obstacle.

It will become clear from the work presented in this paper that Maxworthy's generation mechanism is found to be valid experimentally for the range of parameters considered. We also show that this same mechanism can be found from a numerical model that replaces the interface in a two-layer fluid by a number of point vortices. In more complex stratification than this, it is likely that the lee-wave response will be more complex and that the sequence of events described by Farmer & Smith (1980) will exist.

In §2 we present a description of the laboratory experiments designed to model the production of internal-wave trains by a tidal flow over a two-dimensional obstacle. In §3 two theoretical models are presented. The first is a quasi-steady model based on the steady hydraulic flows discussed by Long (1954). In the second, the vortex-point method is adopted and modified to fit the current problem, in particular to include the presence of irregular boundaries. In §4 the experimental and numerical results are presented and compared. Finally, in §5 a discussion and interpretation of these results is presented.

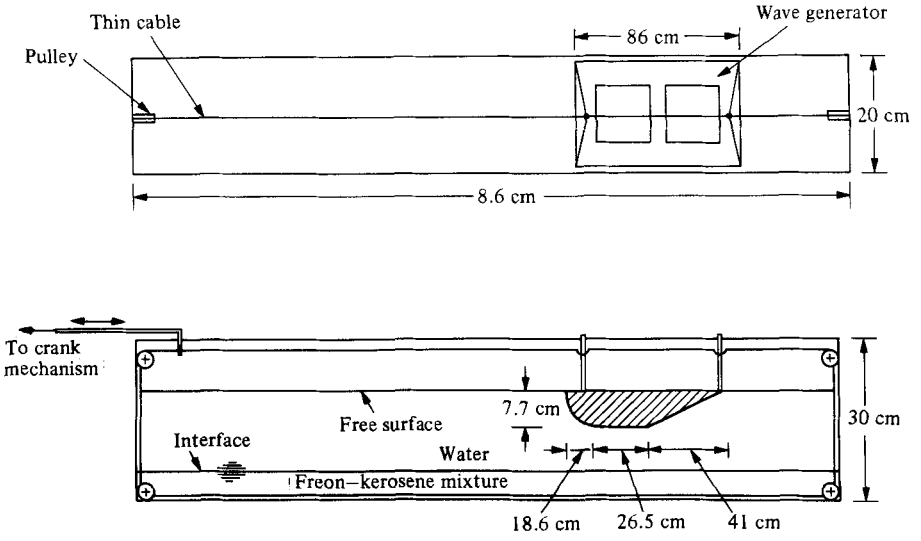

FIGURE 1. Apparatus. For experimental convenience the geometry of the oceanic prototype has been inverted. The topographic feature floats in the upper surface while the equivalent of the mixed layer rests on the bottom of the tank. Tidal flow is simulated by towing the obstacle back and forth using a simple crank–connecting-rod arrangement.

2. Apparatus and procedure

A rectangular Plexiglas channel 8.6 m long, 20 cm wide, and 30 cm deep, as shown in figure 1, was used to maintain a stratified two-layer fluid. This stratification was produced by first filling the channel to the desired depth with the lighter fluid (water). The heavier fluid (a Freon–kerosene mixture of density 1.05 g/cm^2) was then dyed and injected slowly through a funnel placed close to the bottom of the channel.

The wave generator was made by bending a thin Plexiglas top over thicker Plexiglas sheets of the desired shape, that formed the sides of the wave generator. The sides were painted black to improve the quality of the photographs taken of the experiments. The wave generator was 86 cm long, with a maximum depth of 7.7 cm. When it was placed inside the channel, the wave generator extended laterally from one sidewall to the other, except for a small clearance at each side to ensure a free movement. The wave generator could be filled with water to any level in order to control the level to which it could be submerged. The generator was towed through a total stroke of 29 cm by a system of cables and pulleys connected to a simple crank–connecting-rod mechanism driven by a variable-speed motor.

The wave motions that were created by towing the obstacle were observed by photographing the distortions of the dyed lower layer at known intervals of time after the start of the motion, with a camera mounted on a trolley so that all of the waves which were formed were within the field of view at all times.

3. Development of the theoretical model

3.1. *The quasi-steady model*

To model the generation mechanism of the interfacial waves theoretically, we started by using a modification of the steady model developed by Long (1954). In his study of the motion of the steady flow of a two-fluid system over an obstacle, as shown

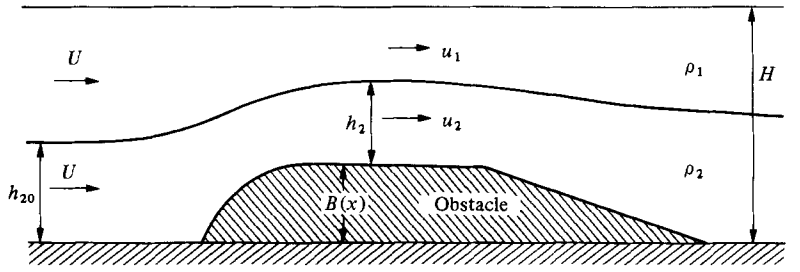

FIGURE 2. Hydrostatic steady model of two-layer flow over an obstacle. In the quasi-steady theory of the lee-wave production by tidal flow it is assumed that the steady flow at each value of the approach stream velocity exists at each instant in the unsteady flow.

in figures 1 and 2, the assumptions of a very small density difference and a hydrostatic pressure distribution were used. We assumed that this steady model was valid at each instant of time in our unsteady flow.

Introduction of the parameters $H' = (H-h_{20})h_{20}/H$, the equivalent depth of the flow; $F_r^2(t) = \rho U^2(t)/(\rho_2-\rho_1)gH'$, the Froude number; $h^*(x) = (H-B(x))/H$, a dimensionless depth of the obstacle at any location; $a^* = (h_{20}-h_2(x)-B(x))/(H-h_{20})$, the dimensionless amplitude of the disturbance at any location x; and finally $R = h_{20}/H$, the ratio of the depth of the two fluid layers, into the continuity and energy equation, yields upon some manipulation

$$h^* = \left[\frac{1+a^*}{R}\right]\left[1 \pm \frac{R/(1-R)}{\left\{1+\dfrac{2a^*(1+a^*)^2}{RF_r^2}\right\}^{\frac{1}{2}}}\right].$$

This equation relates the amplitude of the disturbance to the dimensionless depth of the flow, the Froude number and ratio of the depths of the two fluid layers. In figure 3 the case of $R = 0.6$ and various values of F_r is presented. There are two sets of values of a^* and h^* at which all curves for different values of F_r meet. The first is at $h^* = h_c = 4.2$; here $a^* = 0$, so that the flow is unperturbed, i.e. the obstacle does not exist ($B = 0$). The second is at $h = 0$, where the obstacle blocks the flow completely. For the positive values of a^*, the flow is subcritical and the interface drops over the obstacle. The solution for negative values of a^* is valid when the flow is supercritical and the interface swells over the obstacle. For values of $h^* > h_c$, the height of the obstacle is negative ($B < 0$), i.e. the obstacle is actually replaced by a depression. The flow is supercritical for all positive values of a^* and supercritical for all negative values of a^*.

To compare the results obtained from this quasi-steady model with the experimental results, we assume that this steady solution can be applied at each instant of time, i.e. at each instantaneous value of Froude number, and at this instant the maximum amplitude was found. In figure 4 we present one case just to demonstrate the differences between the quasi-steady solution and the experimental results as a function of time. During the formation of the depression it seems that the experimental amplitude increases linearly with time, while the theoretical amplitude must take a shape that reflects the variations of Froude number. From this and other cases not presented in detail here it is clear that, while the theory might agree with the experiments for small times and for small Froude numbers, it can *never* reproduce the continuously increasing amplitude that was found even when the Froude number

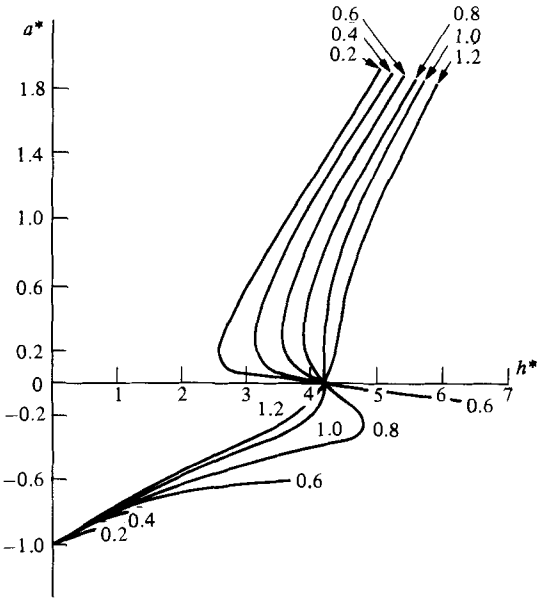

FIGURE 3. Results from the steady equation for $R = 0.6$. Here the dimensionless amplitude a^* and fluid depth L^* are plotted with F_r as parameter.

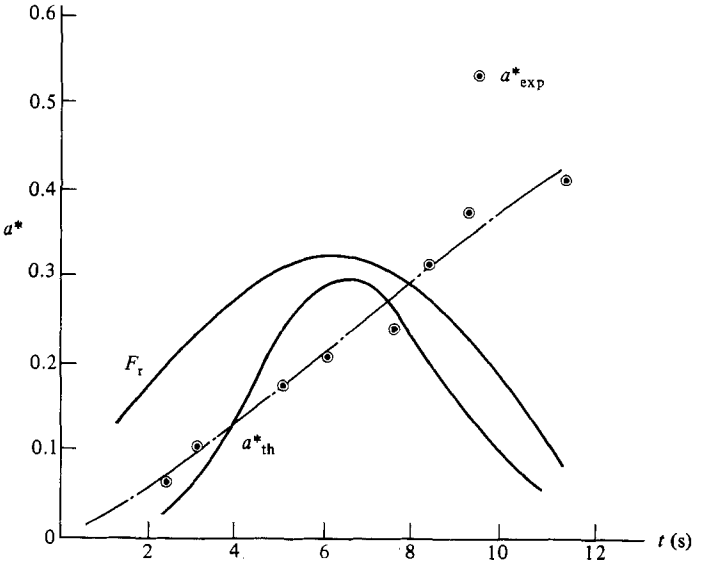

FIGURE 4. Comparison of the experimentally determined maximum amplitude a^*_{exp} and the quasi-steady value as a function of time for $R = 0.9$ and maximum $F_r = 0.33$. The curve of $F_r(t)$ is also shown in order to indicate how its variation and $a^*_{th}(t)$ are closely related in this formulation.

was decreasing. Order-of-magnitude estimates of the time to establish the flow over the obstacle indicate that it is small compared with the tidal period for both model and prototype. However, estimates of both an unsteady and a convective inertia term during the formation of the interface depression indicate that both are of equal importance, and so a quasi-steady model can never be appropriate. In order to

improve our prediction the vortex-point method was adapted to solve the problem of the generation and evolution of interfacial waves numerically.

3.2. *The vortex-point method*

Rosenhead (1931) developed the vortex-point method in order to study Kelvin–Helmholtz instability, that is the flow of uniform density ρ and velocity U, above a stream of the same density but velocity U in the opposite direction. The surface of discontinuity between the two layers was represented by a vortex sheet in the idealized model and was then replaced by a distribution of elemental vortices in the numerical calculations. The paths of the vortices were determined by a numerical step-by-step method, while the line joining these vortices, at any time, was assumed to be an approximation to the actual shape of the surface of discontinuity.

Zarodny & Greenberg (1973) used the vortex-point method to describe large-amplitude but non-breaking, two-dimensional, inviscid, incompressible, irrotational water waves. In their model, both the free surface and the flat bottom boundary were represented by vortex sheets.

More recently, Baker, Meiron & Orszag (1980) have treated the problem of the growth of Rayleigh–Taylor instability to a large amplitude in an inviscid, incompressible, layered flow. The vortex-point method was applied to study the time evolution of an initial sinusoidal disturbance. The governing equations of motion were solved iteratively. The time-stepping was done using the implicit fourth-order Adams–Moulton method that requires only two time derivatives at each time step. The numerical results were in agreement with the results obtained by a conformal-mapping method.

The work done by Baker *et al.* was a good starting point to investigate our problem of interest, namely the generation and evolution of interfacial waves in a stratified medium with a flat rigid boundary at the top and a moving obstacle at the bottom.

3.3. *Problem formulation*

The present flow is modelled by assuming it to be two-dimensional inviscid and incompressible while vorticity is generated at the interface owing to the existence of a tilted surface across which there is a density jump and shear.

The density interface between the two fluid layers can then be represented by a vortex sheet, as shown in figure 5 (*a*). The normal velocity components are continuous across this curve, while there is a jump in tangential velocity components. This jump is the strength of the vortex sheet. The velocity of the sheet, defined as the average fluid velocity of a given point, is given by the Biot–Savart integral as a function of the vortex strengths and the relative positions of all of the other vortices. The equations of motion will be written in Eulerian form and then transformed into the Lagrangian form.

Let

$$Z = x + \mathrm{i}y, \tag{3.1}$$

$$q = u + \mathrm{i}v, \tag{3.2}$$

where Z is the complex position vector of any vortex point and q is its complex velocity vector. The functions x and y are dependent on the Lagrangian variable e (see figure 5*a*; Baker *et al.* 1980, Lansing 1981) that represents the interface and time T. Let

$$\hat{\gamma} = U_{2s} - U_{1s}, \tag{3.3}$$

$$U_{1n} = U_{2n} = U_n, \tag{3.4}$$

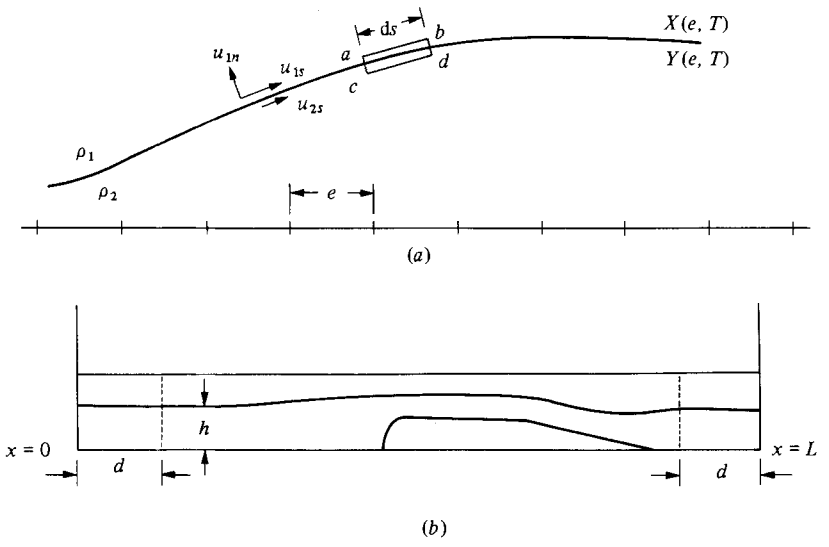

FIGURE 5. (*a*) Numerical model in which the interface is replaced by a series of vortices. (*b*) Defining sketch for regions used to dampen wave energy at the ends of the tank.

where $\hat{\gamma}$ is the vortex-sheet strength and U_{1n} and U_{2n} are the normal components of velocities and U_{2s} and U_{1s} the tangential velocities in the top and bottom layers at the interface.

The distance measured along the vortex sheets is given by

$$s^2 = x^2 + y^2. \tag{3.5}$$

The Biot–Savart law is written as

$$q^*(s) = \frac{-\mathrm{i}}{2\pi} \int_{\mathrm{P}} \frac{\gamma(s')}{Z(s) - Z(s')} \mathrm{d}s' \tag{3.6}$$

(P indicates the principal part of the integral). Here q^* is the complex conjugate of the velocity q and

$$\frac{\mathrm{d}Z}{\mathrm{d}T} = q, \tag{3.7}$$

while

$$\gamma = \frac{\mathrm{d}s}{\mathrm{d}e} \hat{\gamma}, \tag{3.8}$$

where γ is the vortex strength in Lagrangian space and e is the Lagrangian variable. The next step is to find the evolution of γ with time T, i.e. $\mathrm{d}\gamma/\mathrm{d}T$. This is done by evaluating the momentum equation in the tangential direction on either side of the vortex sheet (i.e. the interface) as follows, in both Eulerian and Lagrangian forms. The Eulerian form for the top fluid layer is

$$\rho_1 \left[\frac{\partial U_{1s}}{\mathrm{d}T} + U_{1s} \frac{\partial U_{1s}}{\partial s} + U_{1n} \frac{\partial U_{1s}}{\partial n} \right] = -\frac{\partial p}{\partial s} - \rho_1 g \frac{\partial y}{\partial s}, \tag{3.9}$$

and that for the bottom layer is

$$\rho_2 \left[\frac{\partial U_{2s}}{\partial T} + U_{2s} \frac{\partial U_{2s}}{\partial s} + U_{2n} \frac{\partial U_{2s}}{\partial n} \right] = -\frac{\partial p}{\partial s} - \rho_2 g \frac{\partial y}{\partial s}. \tag{3.10}$$

Introducing the average tangential velocity

$$U_s = \tfrac{1}{2}(U_{1s} + U_{2s}), \tag{3.11}$$

and transforming the momentum equations to the Lagrangian form, where

$$\frac{\mathrm{d}}{\mathrm{d}T} = \frac{\partial}{\partial T} + U_s \frac{\partial}{\partial s} + U_n \frac{\partial}{\partial n}, \tag{3.12}$$

then dividing (3.9) by ρ_1 and (3.10) by ρ_2 and subtracting, the following equation is obtained:

$$\frac{\mathrm{d}\hat{\gamma}}{\mathrm{d}T} + \hat{\gamma}\frac{\partial U_s}{\partial s} = \left[\frac{1}{\rho_1} - \frac{1}{\rho_2}\right]\frac{\partial p}{\partial s}. \tag{3.13}$$

Now converting to the Lagrangian variable e, this equation is written as

$$\frac{\mathrm{d}\gamma}{\mathrm{d}T} = \left[\frac{1}{\rho_1} - \frac{1}{\rho_2}\right]\frac{\mathrm{d}p}{\mathrm{d}e}. \tag{3.14}$$

This equation describes the relation between the pressure distribution and generation of vorticity.

Eliminating the pressure term through some manipulation of these equations (Lansing 1981) yields

$$\frac{\mathrm{d}\gamma}{\mathrm{d}T} = 2A\left[(x_e U_T + y_e v_T) + \frac{1}{8}\frac{\mathrm{d}}{\mathrm{d}e}\left(\frac{\gamma}{S_e}\right)^2 + g y_e\right], \tag{3.15}$$

where $A = (\rho_1 - \rho_2)/(\rho_1 + \rho_2)$ and the subscripts e and T represent differentiation with respect to these quantities. Then (3.15) becomes in complex form

$$\frac{\mathrm{d}\gamma}{\mathrm{d}T} = 2A\left[\mathrm{Re}\,(Z_e q_T^*) + \frac{1}{8}\frac{\mathrm{d}}{\mathrm{d}e}\left(\frac{\gamma}{S_e}\right)^2 + \mathrm{Im}\,(g Z_e)\right]. \tag{3.16}$$

Also, the Biot–Savart integral can be written in the Lagrangian form as

$$q^*(e) = -\frac{\mathrm{i}}{2\pi}\int_{\mathrm{P}} \frac{\gamma(e')}{Z(e) - Z(e')}\,\mathrm{d}e'. \tag{3.17}$$

Accordingly, the acceleration of the vortex sheet is expressed as

$$\frac{\mathrm{d}q^*(e)}{\mathrm{d}T} = -\frac{\mathrm{i}}{2\pi}\left[\int_{\mathrm{P}} \frac{\mathrm{d}\gamma(e')/\mathrm{d}T}{Z(e) - Z(e')}\,\mathrm{d}e' - \int_{\mathrm{P}} \frac{\gamma(e')\{q(e) - q(e)'\}}{\{z(e) - Z(e')\}^2}\,\mathrm{d}e'\right]. \tag{3.18}$$

The total time derivatives are Lagrangian with respect to the sheet velocity (u, v). The right-hand-side of (3.17) describes the baroclinic creation of vorticity. The two main effects included here are the creation of vorticity by gravity, and the generation of vorticity due to the tangential acceleration of the interface. Since the velocity components u and v are related to the vortex-sheet strength γ through the Biot–Savart integral, (3.16) is an integro–differential equation for γ. Equations (3.16)–(3.18) describe the evolution of vorticity and the position of the vortices.

The modelling of the boundaries

The previous formulation is only valid for two superimposed layers of infinite depth. To model the boundaries, including the complex shape of the wave generator, the previous equations must be modified to include their effects, the following assumptions being made, utilizing the solution given by Jaswon & Symm (1977).

(1) The wave generator is represented by a rigid fixed obstacle at each time step that has the surface ∂B.

(2) The flow over the obstacle is irrotational.

(3) The obstacle perturbs the steady flow defined by its velocity potential ψ, and the perturbation potential is ϕ.

(4) The obstacle can be represented by a continuous distribution of sources of density $\sigma(\boldsymbol{R})$ at $\boldsymbol{R} \in \partial B$ extending over a simple curve ∂B. These sources generate a simple layer potential that takes the form

$$\phi(\boldsymbol{P}) = \frac{1}{2\pi} \int_{\partial B} g(\boldsymbol{P}, \boldsymbol{R})\, \sigma(\boldsymbol{R})\, \mathrm{d}\boldsymbol{R} \quad (\boldsymbol{P} \in B_e + \partial B),$$

where B_e is the infinite domain exterior to ∂B. The potential $\phi(\boldsymbol{P})$ is continuous everywhere and has the asymptotic behaviour

$$\phi(\boldsymbol{P}) = O(|\boldsymbol{P}|^2) \quad \text{as} \quad \boldsymbol{P} \to \infty.$$

This means that the simple layer potential ϕ ensures that the perturbation of the fluid flows decays to zero rapidly at infinity and applies only to subcritical flows.

If ϕ is the perturbation potential, so that the resultant velocity potential is $\phi + \psi$, the physical requirement that the component of fluid velocity, normal to the rigid boundary, must be zero implies that

$$\phi'(\boldsymbol{P}) = -\psi'(\boldsymbol{P}) \quad (\boldsymbol{P} \in \partial B).$$

The source density $\sigma(\boldsymbol{P})$ is the unique solution of the integral equation

$$\frac{1}{2\pi} \int_{\partial B} g'(\boldsymbol{P}, \boldsymbol{R})\, \sigma(\boldsymbol{R})\, \mathrm{d}\boldsymbol{R} + \frac{\sigma(P)}{2} = -\psi'(\boldsymbol{P}) \quad (\boldsymbol{P} \in \partial B), \tag{3.19}$$

where $\psi'(\boldsymbol{P})$ is the normal component of the perturbation potential. Define

$$\psi' = \frac{\partial \psi}{\partial x}\frac{\partial x}{\partial n} + \frac{\partial \psi}{\partial y}\frac{\partial y}{\partial n} \tag{3.20}$$

$$= u_B \frac{\partial x}{\partial n} + v_B \frac{\partial y}{\partial n} \tag{3.21}$$

(where u_B and v_B are the components of the velocity induced by the sheet at the boundary, and $\partial x/\partial n$ and $\partial y/\partial n$ are the direction cosines of the normal directed into the boundary B) and taking into consideration the motion of the boundary in the x-direction, then

$$\psi' = \{u_B + U_0 \sin \omega T\} \frac{\partial x}{\partial n} + v_B \frac{\partial y}{\partial n}. \tag{3.22}$$

Introducing the complex notation $q_B^* = u_B - \mathrm{i} u_B$, $\mathrm{d}Z_B/\mathrm{d}e = \mathrm{d}x_B/\mathrm{d}e + \mathrm{i}\, \mathrm{d}y_B/\mathrm{d}e$, where Z_B is the complex position of the boundary, then

$$-\psi' = \mathrm{Im}\,[Z_{Be}\{q_B^* + U_0 \sin \omega T\}]. \tag{3.23}$$

The first term of (3.19) can be rewritten as

$$g'(\boldsymbol{P}, \boldsymbol{R}) = \frac{\partial g}{\partial x}\frac{\partial x}{\partial n} + \frac{\partial g}{\partial y}\frac{\partial y}{\partial n}. \tag{3.24}$$

In two dimensions the kernel $g(\boldsymbol{P}, \boldsymbol{R})$ takes the form

$$g(\boldsymbol{P}, \boldsymbol{R}) = \ln |\boldsymbol{P} - \boldsymbol{R}|. \tag{3.25}$$

Substituting into (3.24),

$$g'(\boldsymbol{P},\boldsymbol{R}) = \left[\frac{\partial}{\partial x}\ln|\boldsymbol{P}-\boldsymbol{R}|\right]x' + \left[\frac{\partial}{\partial y}\ln|\boldsymbol{P}-\boldsymbol{R}|\right]y', \tag{3.26}$$

where

$$x' = \frac{\partial x}{\partial n}, \quad y' = \frac{\partial y}{\partial n}.$$

Differentiating and substituting for x' and y',

$$g'(\boldsymbol{P},\boldsymbol{R}) = -\frac{yB_e(x-x_R)+xB_e(y-y_R)}{|\boldsymbol{P}-\boldsymbol{R}|^2}, \tag{3.27}$$

where x, y and the components of the vector $\boldsymbol{P}$, and x_R, y_R are the components of the vector $\boldsymbol{R}$. Equation (3.27) can be rewritten as

$$g'(\boldsymbol{P},\boldsymbol{R}) = -\operatorname{Im}\left[\frac{\Delta Z_{Be}}{\Delta Z_B}\right]. \tag{3.28}$$

Substituting into (3.19), and using the Lagrangian frame of reference,

$$\operatorname{Im}[Z_{Be}(q_B^* + U_0\sin\omega T)] = -\frac{1}{2\pi}\operatorname{Im}\left[Z_{Be}\,\mathrm{P}\int\frac{\sigma(e')\,de'}{Z_B(e)-Z_B(e')}\right]+\frac{\sigma(e)}{2} \tag{3.29}$$

or

$$\sigma(e) = \operatorname{Im}\left\{Z_{Be}\left[\frac{1}{\pi}\int_P\frac{\sigma(e')}{Z_B(e)-Z_B(e')}+2(q_B^*+U_0\sin\omega T)\right]\right\}. \tag{3.30}$$

Away from the boundary $\sigma(e) = 0$, $Z_B(e) = Z(e)$ and the boundary velocity $U_0\sin\omega T$ will equal zero so that (3.30) becomes

$$q_B^*(e) = -\frac{1}{2\pi}\int_P\frac{\sigma(e')}{Z(e)-Z_B(e')}. \tag{3.31}$$

Note that q_B^* is the modifying term to the interface velocity.

The total velocity at the interface will be composed of two parts: the velocity of the vortex sheet found from the Biot–Savart integral, and the modifying velocity that is the velocity due to the source distribution of the rigid boundaries:

$$q^*(e) = -\frac{\mathrm{i}}{2\pi}\int_P\frac{\gamma(e')}{Z(e)-Z(e')}de' + \frac{1}{2\pi}\int_P\frac{\sigma(e')}{Z(e)-Z_B(e')}de'. \tag{3.32}$$

In addition, the acceleration at the interface is the total time derivative of the previous equation, i.e.

$$\frac{dq^*(e)}{dT} = -\frac{\mathrm{i}}{2\pi}\left\{\int_P\frac{d\gamma(e')/dT}{Z(e)-Z(e')}de' - \int_P\frac{\gamma(e')\,[q(e)-q(e')]}{[Z(e)-Z(e')]^2}de'\right\}$$
$$+\frac{1}{2\pi}\left\{\int_P\frac{d\sigma(e')/dT}{Z(e)-Z_B(e')}de' - \int_P\frac{\sigma(e')\,[q(e)-U]}{[Z(e)-Z_B(e')']^2}de'\right\}. \tag{3.33}$$

Equation (3.33) is a function of σ and its time derivative, which is found by differentiating (3.32) with respect to time:

$$\frac{d\sigma(e)}{dT} = \operatorname{Im} Z_{Be}\left[\frac{1}{\pi}\int_P\frac{d\sigma(e')/dT\,de'}{[Z_B(e)-Z_B(e')]^2}+2\frac{d}{dT}q_B^*+2U_0\,\omega\cos\omega T\right]. \tag{3.34}$$

The velocity q_B^* is found from the Biot–Savart integral at (x_B, y_B). Note that q_B^* is the velocity of the flow at the boundaries:

$$q_B^* = -\frac{i}{2\pi}\int_P \frac{\gamma(e')}{Z_B(e)-Z(e)}\,de' \tag{3.35}$$

or

$$\frac{d\sigma(e)}{dT} = \mathrm{Im}\left\{Z_{Be}\left[\frac{1}{\pi}\left(\int_P \frac{d\sigma(e')/dT}{Z_B(e)-Z_B(e')}\,de' - i\int_P \frac{d\gamma(e')/dT}{Z_B(e)-Z(e')}\,de' + i\int_P \frac{\gamma(e')\,[U-q(e')]}{[Z_B(e)-Z(e')]^2}\,de'\right) + 2U_0\,\omega\cos\omega T\right]\right\}. \tag{3.36}$$

The acceleration of the boundaries, $U_0\,\omega\cos\omega T$, is the main contributing term to $d\sigma(e)/dT$, especially when $d\sigma(e')/dT$, $\gamma(e')$ and $d\gamma(e')/dT$ are equal to zero at $T = 0$.

Equations (3.16) and (3.36) are two simultaneous ordinary differential equations in $d\gamma/dT$ and $d\sigma/dT$, so that with the addition of (3.7), the evolution of vortex-sheet strength, its position and source density are well defined.

3.4. *The radiation conditions*

Owing to the need to confine the vortex sheet to a finite domain, we must take special precautions to prevent wave reflection from the ends of this region. This is accomplished by introducing very viscous boundary layers at each end of the channel as shown in figure 5(*b*) to dampen the vortex strength, its vertical position y and density of the source. In these regions we assume

$$\frac{dy}{dT} = v - \frac{a}{d^2}(x-L+d)^2\,(y-h), \tag{3.37}$$

$$\left.\frac{d\gamma}{dT}\right|_{\text{corrected}} = \frac{d\gamma}{dT} - \frac{a}{d^2}(x-L+d)^2\,\gamma, \tag{3.38}$$

$$\left.\frac{d\sigma}{dT}\right|_{\text{corrected}} = \frac{d\sigma}{dT} - \frac{a}{d^2}(x-L+d)^2\,\sigma, \tag{3.39}$$

where a is the internally computed dampening factor, d the dampening length and h the undisturbed depth of the interface.

3.5. *Numerical computations*

The first step of the numerical solution of the vortex-point method was the subdivision of the interface into small equal sections. These sections were simply equal intervals of plane curves. At each of the interval points, the position Z and the vortex-sheet strength were found. Initially, the undisturbed interface was represented by the complex vector Z, while γ was assumed to be zero.

To find the perturbation velocity and acceleration due to the presence of the wave generator, the first step was the subdivision of the boundary (obstacle) ∂B into suitably small sections. In two dimensions these sections were also equal, smooth plane curves.

The best choice of the interval points was to include any corner of ∂B or any point that describes any change in ∂B. This ensured that each section or interval was smooth so that the normal was well defined at each nodal point, and so that a simple boundary condition applied within each interval.

The numerical computations proceeded as follows. First, the vortices were

distributed at equal spacing at the interface. The same was done for the sources that represent the rigid boundaries.

Initial values of γ, σ, $d\gamma/dT$ and $d\sigma/dT$ were assumed to be zero. The velocity of the interface was then calculated using (3.32). Next, $d\sigma/dT$ and $d\gamma/dT$ were calculated by iteration. The iteration began by calculating $d\sigma/dT$ from (3.36), followed by the acceleration of the interface, as calculated from (3.33). The acceleration value was then substituted into (3.16) to find $d\gamma/dT$. The new value of $d\gamma/dT$ was then used to calculate the new value of $d\sigma/dT$, and the procedure was repeated until the errors in both $d\gamma/dT$ and $d\sigma/dT$ were within the permissible limits. The radiation conditions were applied at each time step. After calculating the velocity of the interface, $d\sigma/dT$ and $d\gamma/dT$, the integration procedure followed by finding the new values, for these parameters, at the next time step. The time stepping was done by using the implicit fourth-order Adams–Moulton method. Because this method is not a self-starter, the first three time steps were computed by the Runge–Kutta method.

The Adams–Moulton technique was found to be stable and fast. For each time step, only two evaluations of the time derivatives were required, compared with the four evaluations required for the Runge–Kutta method. The required computer memory is of the order of $N+N_B$, where N is the number of vortices and N_B is the number of sources. About N^2 arithmetic operations at each step are needed. The computer system used in these computations is the TOPS-20 at U.S.C.

4. Experimental and numerical results

4.1. *Experimental results*

In all cases considered, we will use the same definitions as in §3 for Froude number F_r and the ratio R of depths. The limits of the ratio R, during experiments, were constrained by: (*a*) the depth of the Freon–kerosene mixture (2.90 cm) and (*b*) the depth of the fresh-water layer (which was varied from 9.80 to 14.30 cm). The choice of the minimum fresh-water depth was based on the deepest section of the wave generator (7.70 cm) to avoid blocking. The ratio R was varied for each experiment and could be measured to an accuracy of ± 0.005. The Froude number, since it is time-dependent, changes from zero to a maximum then back to zero again, for the one-half sinusoidal path; while for the full-sinusoidal path it changes sign over the second half of the period of motion and the obstacle returns to its starting position.

The experimental results presented in figures 6–10 are categorized according to: (1) the ratio R; (2) the maximum Froude number (computed at the maximum speed) for the same R; and (3) the motion history of the wave generator. For the sake of clarity, only one parameter was varied at a time. For instance, in figure 6, the obstacle was towed for one half-period of the sinusoidal path where R is kept at 0.815 and the maximum Froude number at 0.655. Figure 7 represents the motion for the same R and F_r as in the previous case, but for the full sinusoidal path. Figure 9 shows the wave motion for $R = 0.770$ and maximum $F_r = 0.670$, for one-half of the sinusoidal path, while figure 10 shows the same case, but for the full sinusoidal path. In all cases we consider certain dependent variables which are characteristic of that particular experiment, such as the wave amplitude, length, phase speed and growth rate, and whether or not mixing occurs. We then determine how these parameters vary as the independent parameters are changed.

For the case of the full sinusoidal path, the wave amplitude is larger, the slope of the generated wave is steeper, the length of the wave front is longer, the phase speed

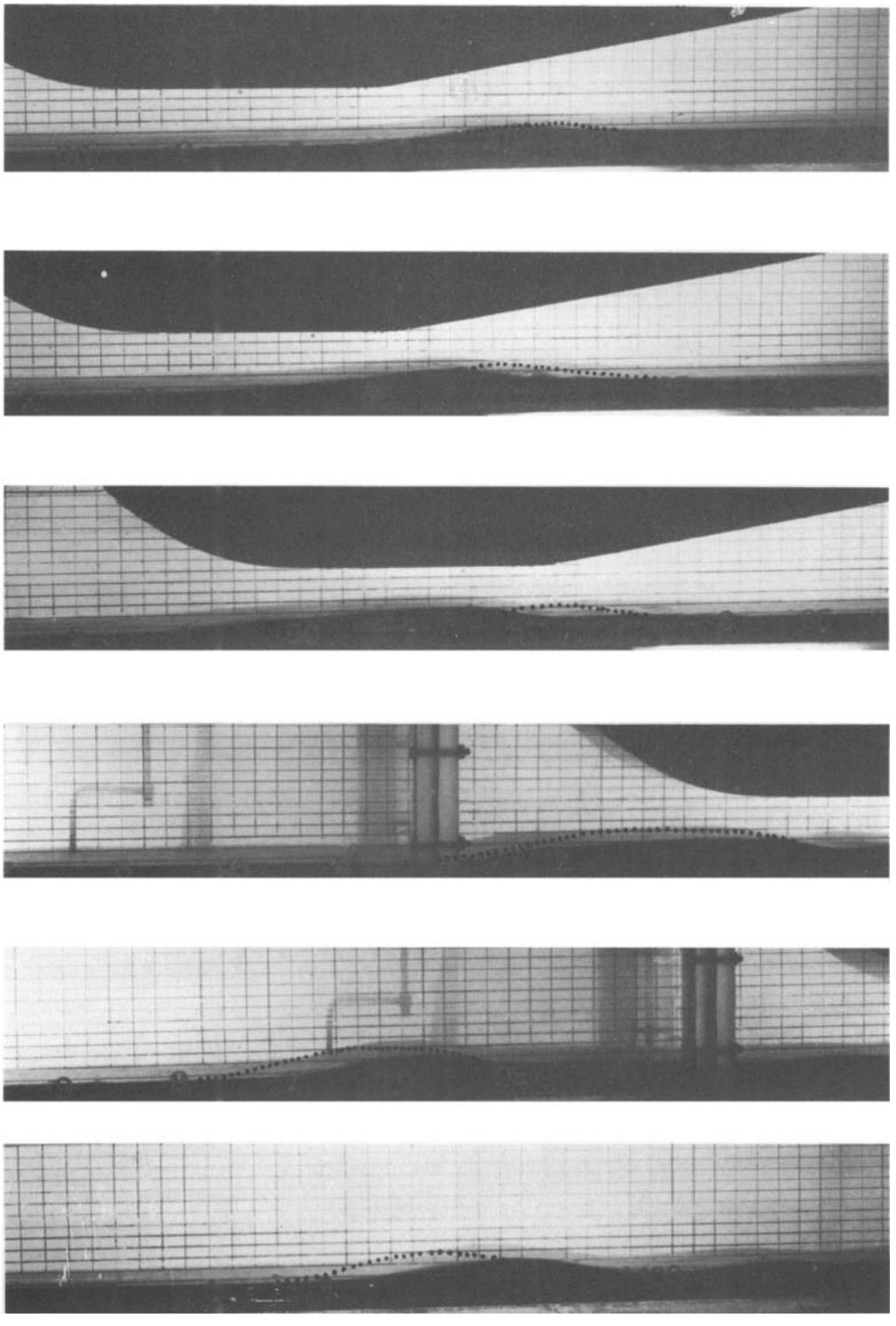

FIGURE 6. Experimental results for $R = 0.815$, maximum $F_T = 0.655$ and one-half of a sinusoidal motion of the obstacle of full period 12.9 s. From top to bottom the photographs were taken 4.1, 6.6, 8.8, 10.2, 14.6 and 18.9 s from the start of the motion. The dotted lines in this and the figures that follow represent the numerically determined surface shape as discussed in detail in §4.4, while the background scale has separations of 1 cm vertically and 2 cm horizontally.

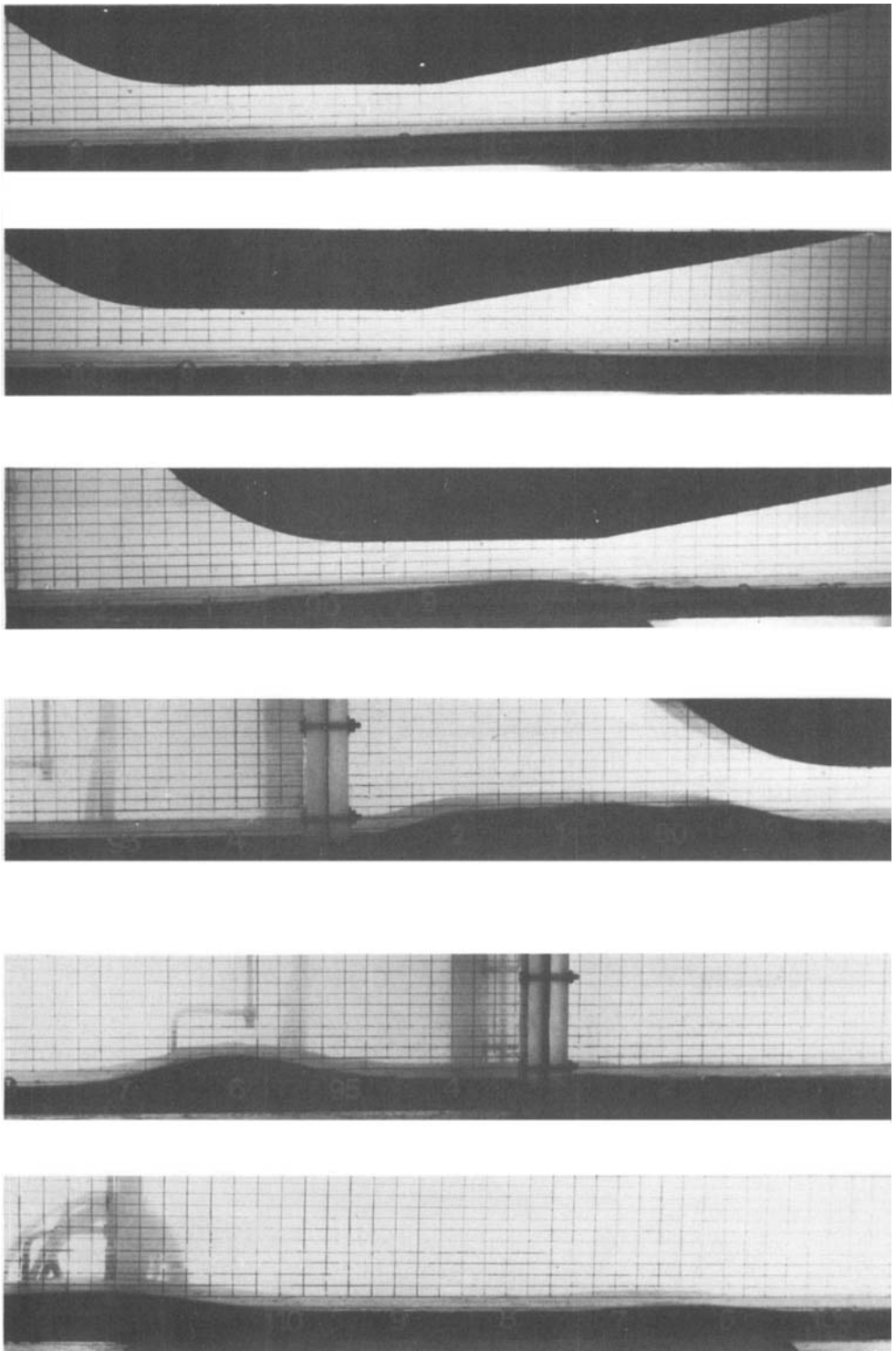

FIGURE 7. Experimental results for $R = 0.815$ and maximum $F_r = 0.655$ for one full sinusoidal period of obstacle motion of period 12.9 s. Photographs were taken 1.0, 2.8, 6.1, 8.0, 12.2 and 26.0 s from the start of the motion.

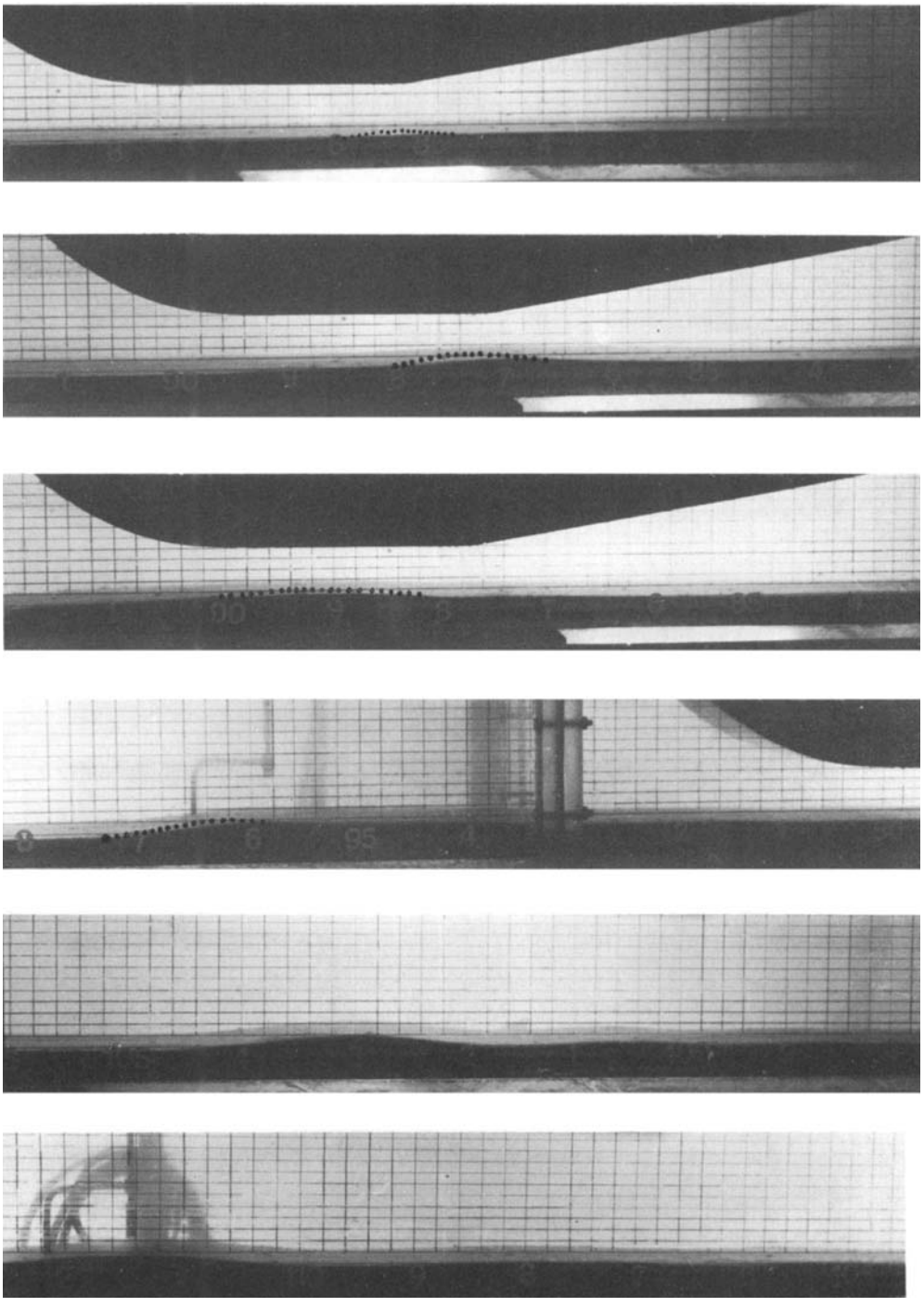

FIGURE 8. Experimental results for $R = 0.815$, maximum $F_r = 0.327$ and one-half of a full sinusoidal period of 25.9 s. Photographs were taken 6.3, 8.8, 12.0, 17.4, 23.1 and 29.7 s from the start of the motion.

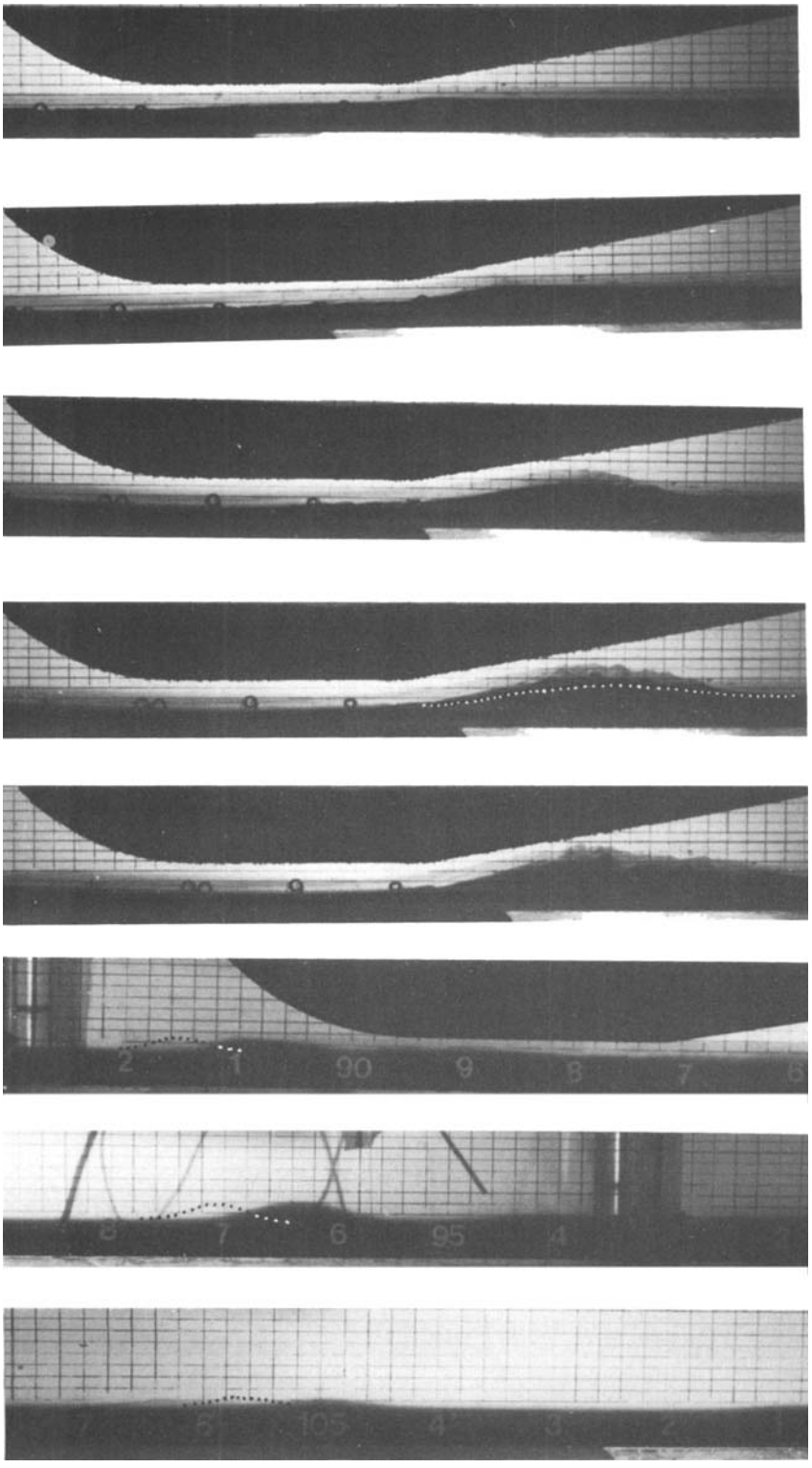

FIGURE 9. Experimental results for $R = 0.770$, maximum $F_r = 0.670$ and one-half of a full sinusoidal period of 12.9 s. Photographs were taken 1.1, 2.3, 3.1, 4.5, 5.4, 9.0, 12.6 and 18.6 s from the start of the motion.

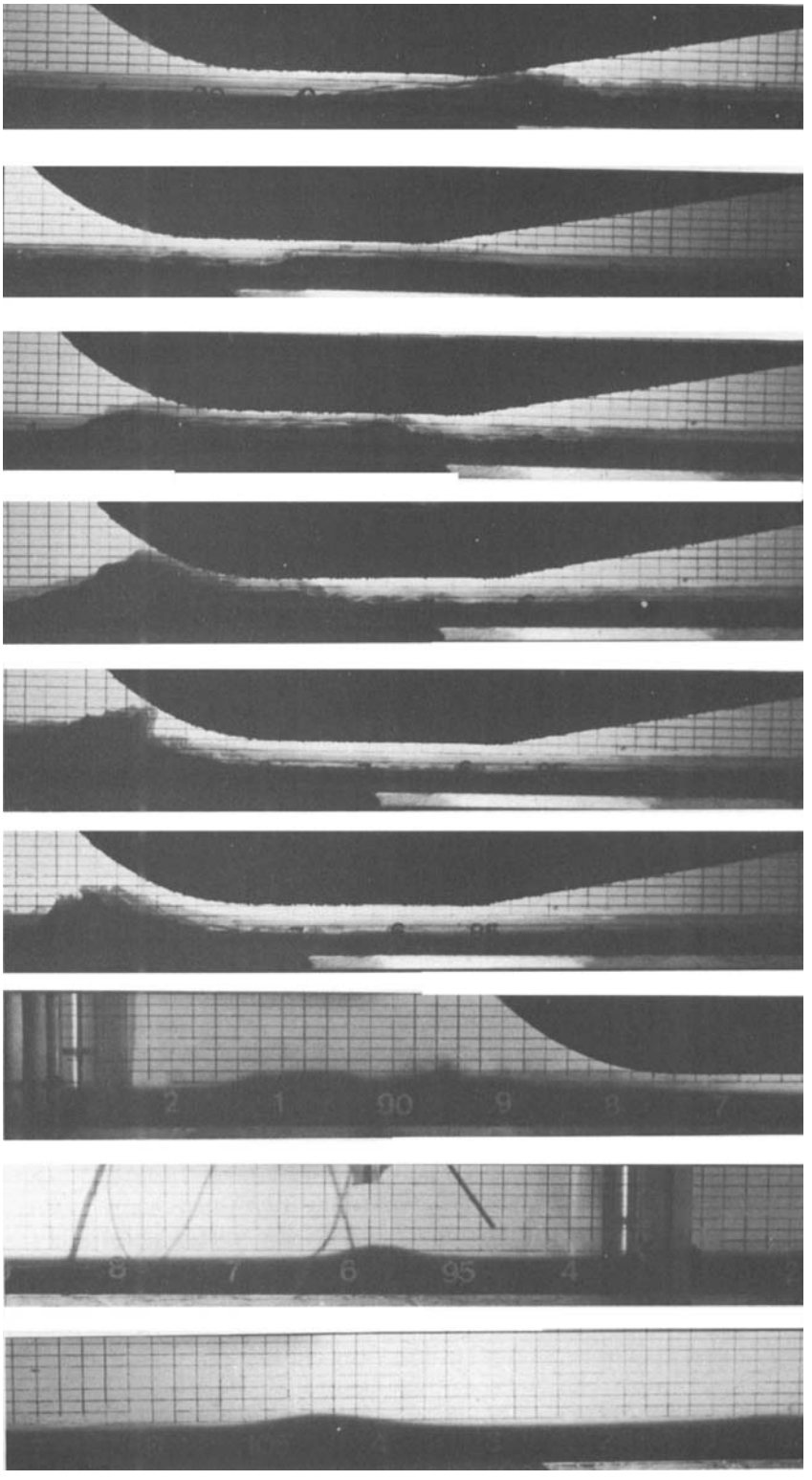

FIGURE 10. Same as figure 9, except for one full sinusoidal period. Photographs were taken 7.8, 8.6, 9.1, 10.1, 11.2, 15.3, 17.0, 22.3 and 31.3 s from the start of the motion.

is larger, and the growth rate of the generated wave is higher than the half-path case. In both cases, shown in figures 9 and 10, mixing occurs. The case of full sinusoidal path, figure 10, shows the separation of two solitons. The phase speed for the case of the full sinusoidal path is larger than that of the half-path until the separation of the two solitons takes place, after which the phase-speed trend is reversed.

To study the effect of the maximum Froude number on the wave motion, the maximum speed was varied while fixing R for one-half of the sinusoidal path. The wave motion in figure 8 should be compared with that in figure 6. It is observed that, as the maximum Froude number increases, the maximum amplitude also increases, while mixing occurs at the larger Froude number.

To examine the effect of changing the ratio R only, two cases shown in figures 6 and 9 are compared, since they have the same Froude number (approximately) and the same one-half sinusoidal path. The most significant observations are as follows:

(1) mixing occurs in the cases of smaller R;

(2) the growth rate of the lee wave increases as R decreases; however, the reduction of the wave amplitude is clearly shown in the cases of smaller R due to the occurrence of mixing;

(3) the slope of the wave front increases as R decreases;

(4) the wave amplitude increases as R decreases;

(5) the number of waves generated increases as R is decreased.

Consider the case where the ratio R is kept at 0.770 and the maximum Froude number F_T at 0.670. Figure 9 shows both the generation and the evolution of the internal waves when the obstacle is towed for one half-period of the sinusoidal path. Figure 10 then illustrates the continuation of the wave motion of figure 9 where the time recording begins during the second half of the obstacle motion to complete the sinusoidal path. Waves generated in this case have the maximum in the amplitude, slope, phase speed and growth rate. Mixing occurs in the lee of the obstacle as shown in both figures 9 and 10. Also, the interaction of waves and intense mixing takes place on the other side of the obstacle only in the case of a full period of the sinusoidal path.

4.2. *Numerical results*

Having observed the wave generation and evolution experimentally, a comparison can be made with the numerical computations, based on the numerical integration technique previously presented in §3. The interface was modelled by 200 discrete vortices, while the boundaries, both at the top and the bottom, were modelled by a total of 200 sources. Placing the obstacle as a part of the bottom boundary provided some numerical convenience. The bottom boundary remained unchanged while the top rigid flat boundary was moved upward or downward depending on the ratio required. Accordingly, the position of the interface had to be moved upward or downward to maintain the correct depth of the two layers.

The requirement that the distance between any two consecutive vortices should be less than or equal to $\frac{2}{3}$ of the distance between any vortex point and its nearest boundary, dictated that the initial distance between any two consecutive vortices should be about 2 cm or less. Note that the minimum distance between any vortex point and a source was 2.9 cm. Consequently, the interface length was limited, in the computation, to 4 m. The section of interest was chosen to begin 50 cm downstream from the obstacle and to end 260 cm upstream of it to allow enough space for wave evolution. The length of the dampening layer was assumed to be 30 cm at each end of the channel. The arclength between any two consecutive sources was taken as 4 cm, and was kept constant. In all the cases modelled, the following variables were used:

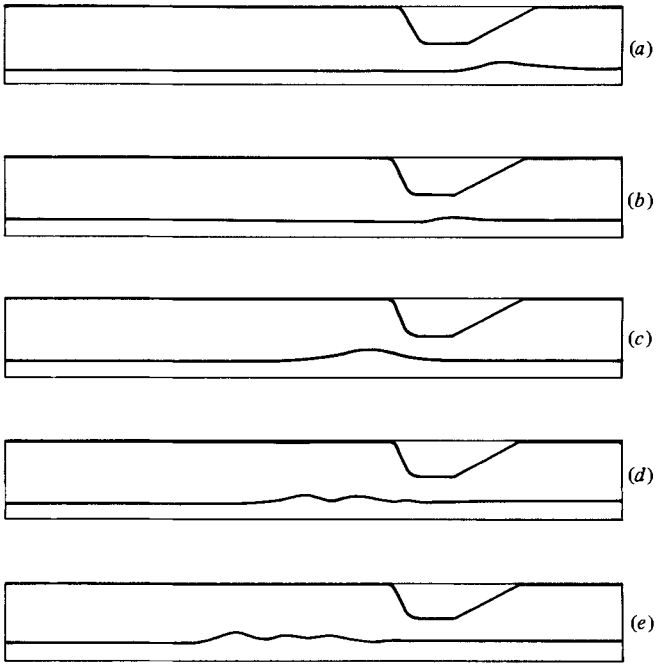

FIGURE 11. Theoretical interface shape for $R = 0.815$, maximum $F_r = 0.655$ and one-half of a full sinusoidal period of 12.9 s. The times for each figure are: (*a*) 4.0 s; (*b*) 8.0 s; (*c*) 11.0 s; (*d*) 14.0 s; (*e*) 1.0 s.

$\rho_1 = 1.0$ g/cm^3, $\rho_2 = 1.05$ g/cm^3, and acceleration due to gravity $g = 981$ cm/s^2. The size of the time step and the dampening factor a, were internally calculated by the computer program. It was found that the larger the Froude number, the smaller the time step should be for smaller computational round-off errors.

To avoid the singularities that might occur during the integration of the Biot–Savart integral, the integration was performed by evaluating the integrand at alternate sets of points using the trapezoidal rule. For example, when the velocity was determined at an odd point, point 1 say, the integration was performed for the following even points (e.g. points 2, 4, 6, ...). Similarly, for an even point, the integration was done over all the odd points.

Numerical differentiation (for quantities such as $\mathrm{d}Z/\mathrm{d}e$) can be performed using first a cubic spline fit followed by differentiation. However, it was performed in this work using the forward-difference method for the first point, and the mid-difference method for any point thereafter except for the last point, where the backward-difference method was used. The iteration procedure, for Fredholm's integral of the second kind, is always convergent provided that the interface, its vorticity and source density, of the rigid boundaries are all 'smooth'. It was found that only 12 iterations were sufficient to obtain an accuracy for both the vortex strength and source density to four significant figures, which is the permissible error specified in both σ and γ.

Furthermore, to avoid the possible wave instabilities that might occur during computations, a smoothing technique was used. This technique was developed by Longuet-Higgins & Cokelet (1978). The smoothing technique used two quadratic equations, provided that the displacement of the interface and its velocity were known at two times T_1 and T_2. The same smoothing process was performed on the vortex strength and source density.

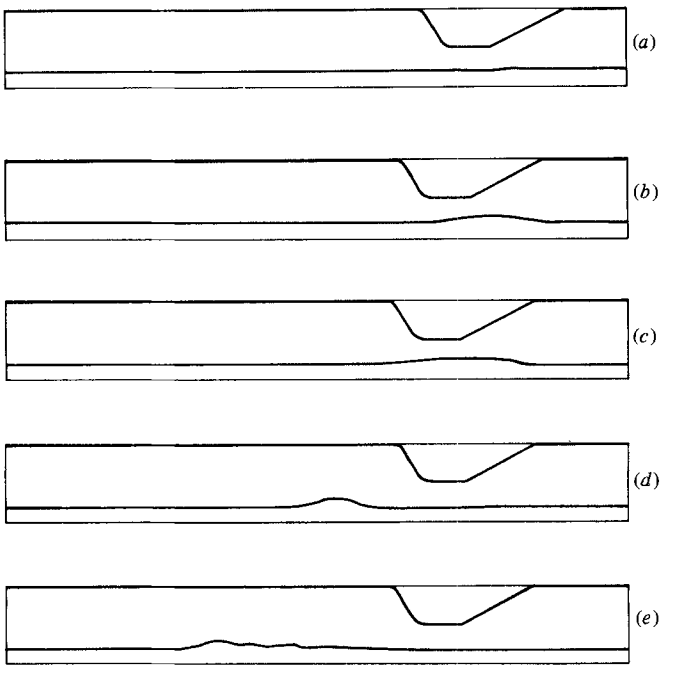

FIGURE 12. Theoretical interface shape for $R = 0.815$, maximum $F_r = 0.327$ and one-half of a full sinusoidal period of 25.9 s. The times for each figure are: (*a*) 4.5 s; (*b*) 9.0 s; (*c*) 11.6 s; (*d*) 17.0 s; (*e*) 24.0 s.

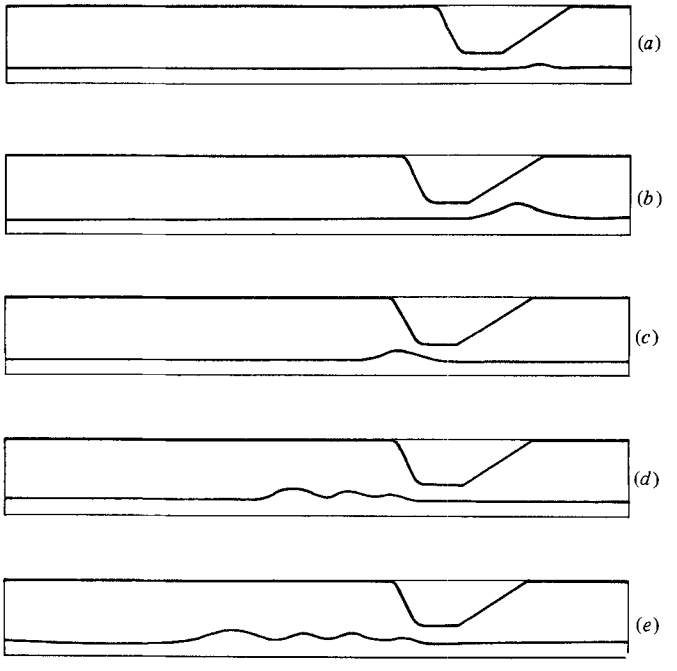

FIGURE 13. Theoretical interface shapes for $R = 0.770$, maximum $F_r = 0.672$ and one-half of a full sinusoidal period 12.9 s. The times for each figure are: (*a*) 1.0 s; (*b*) 4.5 s; (*c*) 9.0 s; (*d*) 15.0 s; (*e*) 17.0 s.

The three cases shown in figures 11–13 were chosen and solved numerically for an obstacle motion representing one-half of the sinusoidal path motion. In figures 11 and 12 the maximum Froude number is 0.655 and 0.327 respectively, and R is kept constant at 0.815. As in the corresponding experiments, the larger Froude number produces a larger wave and solitary waves.

For figures 11 and 13 the maximum Froude number is the same (approximately), while $R = 0.815$ and 0.770 respectively. Again, the observations made from experiments show the same trend with larger waves at the smaller value of R.

Although mixing occurs in the experimental results in figures 1 and 9, it must be eliminated in the corresponding numerical solutions shown in figures 11 and 13, in order to achieve convergence, which takes place only when the interface is smooth.

5. Comparison between numerical and experimental results

The comparisons between numerical and experimental results are superimposed on the experimental results shown in figures 6, 8 and 9. We see that even though the amplitudes are of comparable magnitude, there is a difference in the location of the maximum wave amplitude, with the interface position found from the numerical solution having the more advanced phase, in figures 6 and 9. In figure 8 we find agreement between amplitudes and phase speed, wave-front slope and the number of waves, indicating that for small Froude numbers the numerical solution is in complete agreement with the experimental results. However, for larger Froude numbers, there exists a small difference in phase-front location. The possible reasons for the difference in location can be explained as follows.

(1) The velocity of the wave generator (obstacle) was assumed ideally to take the form $U = U_0 \sin \omega T$, where the variables U_0 and ω were obtained from the driving-mechanism data. However, the ratio of crank to connecting-rod length was not small, resulting in a small deviation of the actual velocity form from the sinusoidal shape.

(2) The bottom rigid boundaries in the numerical solution were assumed to extend beyond the obstacle region. This assumption would affect the phase-speed accuracy through source density, since in the experiments the fluid acts as part of the boundary.

(3) Modelling of rigid boundaries by a source distribution is based on the assumption of a steady flow passing over rigid boundaries. The problem treated in this work has moving boundaries with a time-dependent velocity. The source density will affect both the position and the velocity of the interface, which in turn affect the phase speed.

(4) In the experiments the flow may separate from the back slope of the obstacle and present a modified body shape to the outer flow. Such an effect is not included in the numerical model. Also, viscous damping and mixing, which were not taken into account in the numerical calculations, act to decrease the wave amplitude and hence the wave speed in the experiments.

It is evident from the above comparison that there exists, in general, good qualitative and quantitative agreements between the experiments and the numerical simulation. The vortex-point method is a relatively new approach, which can provide a good description and understanding of the complex phenomena of generation and evolution of internal-wave trains in the oceans and the atmosphere under appropriate circumstances.

6. Discussion and conclusions

Based on the results presented in the previous sections, which to a large extent are self-explanatory, we discuss briefly the major findings of this work as follows. The basic mechanisms of wave generation and evolution can be seen in figures 6–10. As the tidal flow passes over the obstacle, a single depression is formed in the lee. The characteristics of this depression depend on the characteristics of the flow, i.e. the Froude number, and the ratio of depths of the fluid layers, as well as the characteristics of the obstacle. The simplest case occurs when the amplitude of the depression is such that no breaking or mixing takes place. Increasing the maximum Froude number and decreasing the ratio R of the depths of the two fluid layers will cause mixing. Consequently, the amplitude of the depression will not be well defined, and only an estimate of its value can be made.

As the velocity of the obstacle decreases, the depression that has gained a large phase speed with respect to the moving fluid, i.e. a large increase in its kinetic and potential energy, will move upstream against the flow, where it loses some of its kinetic energy. Depending on the phase speed of the depression, the path of the obstacle, and the length of the obstacle, the depression may or may not interact with another depression which can be formed on the other side of the obstacle during the obstacle's return motion to its original position.

Similar observations on this phase of motion were reported by Gargett (1976) in the study of large pulses of well-mixed fluid passing over the crest of a submarine ridge on the slackening tide. The pulses created internal waves, and the mixing process was so intense that a well-defined stratification did not occur over the submarine ridge.

As the depression front propagates away from the obstacle, it evolves into a number of internal waves. The internal waves are ordered, in sequence, by their amplitude. The number of internal waves and their amplitude depend on the characteristics of the basic flow and the depression formed.

Farmer & Smith (1980) suggested that the generation of internal wave packets start with a separation of the boundary layers followed by the formation of either a single massive lee wave or a train of lee waves depending on the stratification and the strength of the tidal current.

The sequence of wave motion presented in this study is in agreement with Maxworthy (1979), where only one single depression formed behind the obstacle. No observations of a lee-wave train were made, almost certainly because the ranges of tidal current and stratification values used are limited.

An attempt to use a quasi-steady hydraulic model was not successful and was superseded by a numerical model consisting of a well-defined interface between two constant-density fluid layers that were bounded by two rigid boundaries, one of which was flat and fixed and the other irregular and moving with a sinusoidal velocity. The numerical solution was based on the vortex-point method in which the interface was described by a set of discrete vortices. The baroclinic generation of vorticity in the interface was caused by the existence of a density difference and shear. The flat rigid boundary modified the vertical motion of the interface, while the irregular boundary, including the moving obstacle, acted as a flow-perturbing source. The final governing equations to be solved were two simultaneous integro–differential equations, which primarily yielded the displacement of the interface at different times.

The phase-speed and amplitude results of the model were found to be in complete agreement with the experimental data at small Froude numbers. However, the results diverse slightly in the location of the maximum amplitude only when the Froude number becomes large, for the same ratio R.

An additional attempt was made to check the accuracy and the applicability of the model by comparing the results of a special problem with a known solution from linear theory. We considered the case of two fluid layers bounded by flat boundaries with no shear. The interface was given an initial sinusoidal perturbation and the motion of the wave crests were calculated. The difference in phase speed between linear theory and the numerical calculation was found to be in the order of 9%.

In conclusion, the motion of internal waves cannot be accurately described by a simple quasi-steady buoyancy–inertia balance only; rather, the model should take into account all time-dependent parameters that affect the motion. The vortex-point method has provided a promising approach to the problem and enhanced the understanding of the generation and evolution of internal waves.

The work described here were performed at the University of Southern California under ONR Grant N00014-76-G9211. Casey deVries built the apparatus, and his help is greatly appreciated. The help of Dr Gregory Baker of the University of Arizona on the application of the vortex-point method is gratefully acknowledged.

REFERENCES

Apel, J. R. & Holbrook, J. R. 1980 The Sulu Sea internal soliton experiment. Part A. Background and overview. *EOS* **61**, 1009.

Baker, G. R., Merion, D. I. & Orszag, S. A. 1980 Vortex simulation of the Rayleigh–Taylor instability. *Phys. Fluids* **25**, 1485.

Chereskin, T. K. 1983 Generation of internal waves in Massachusetts Bay. *J. Geophys. Res.* **88**, 2649.

Farmer, D. M. & Smith, J. D. 1980 Tidal interaction of stratified flow with a sill in Knight Inlet. *Deep-Dea Res.* **27A**, 239.

Gargett, A. E. 1976 Generation of internal waves in the Strait of Georgia, British Columbia. *Deep-Sea Res.* **23**, 17.

Halpern, D. 1971 Observation on short period internal waves in Massachusetts Bay. *J. Mar. Res.* **29**, 116.

Holbrook, J. R. & Apel, J. R. 1980 The Sulu Sea internal solitons. Part B. Observation of large-amplitude nonlinear internal waves. *EOS* **61**, 1009.

Jaswon, M. A. & Symm, G. T. *Integral Equation Methods in Potential Theory and Elastostatics.* Academic.

Lansing, F. S. 1981 On the generation and evolution of interfacial waves. Ph.D. thesis, University of Southern California.

Lee, C. Y. & Beardsley, R. C. 1974 The generation of long internal waves in a weakly stratified shear flow. *J. Geophys. Res.* **79**, 453–462.

Liu, A. K. 1981 Internal solitons in the Sulu Sea: comparison of wave theory with field data. *Dynatech Rep.* DT-8204-01.

Long, R. R. 1954 Some aspects of the flow of stratified fluids. II. Experiments with a two-fluid system. *Tellus* **6**, 97.

Longuet-Higgins, M. S. & Cokelet, E. D. 1978 The deformation of steep surface waves on water. II. Growth of normal mode instabilities. *Proc. R. Soc. Lond.* A **364**.

Maxworthy, T. 1979 A note on the internal solitary waves produced by tidal flow over a three dimensional ridge. *J. Geophys. Res.* **84**, 338.

Osborne, A. R. & Burch, T. 1980 Internal soliton in the Andaman Sea. *Science* **208**, 451.

Rosenhead, L. 1931 The formation of vortices from surface discontinuity. *Proc. R. Soc. Lond.* A **134**, 170.

Smith, J. D. & Farmer, D. M. 1977 Nonlinear internal waves and internal hydraulic jump in a fjord. In *Geofluiddynamical Wave Mathematics*, p. 42. University of Washington, Seattle.

Zarodny, S. J. & Greenberg, M. D. 1973 On a vortex sheet approach to the numerical calculation of water waves. *J. Comp. Phys.* **11**, 440.